SCIENCE CHINA
Chemistry

•ARTICLES•

June 2024 Vol.67 No.6: 1990–2001
https://doi.org/10.1007/s11426-024-2055-4

Construction of LiCl/LiF/LiZn hybrid SEI interface achieving high-performance sulfide-based all-solid-state lithium metal batteries

Chaochao Wei[1,2], Yujie Xiao[1], Zhongkai Wu[1], Chen Liu[1], Qiyue Luo[1], Ziling Jiang[1], Lin Li[1], Liang Ming[1], Jie Yang[1], Shijie Cheng[1] & Chuang Yu[1*]

[1] *State Key Laboratory of Advanced Electromagnetic Technology, School of Electrical and Electronic Engineering, Huazhong University of Science and Technology, Wuhan 430074, China;*
[2] *School of Chemistry and Chemical Engineering, Huazhong University of Science and Technology, Wuhan 430074, China*

Received February 16, 2024; accepted April 22, 2024; published online May 11, 2024

Sulfide-based all-solid-state lithium metal batteries (ASSLMBs) have received extensive attention due to their high energy density and high safety, while the poor interface stability between sulfide electrolyte and lithium metal anode limits their development. Hence, a hybrid SEI (LICl/LiF/LiZn) was constructed at the interface between $Li_{5.5}PS_{4.5}Cl_{1.5}$ sulfide electrolyte and lithium metal. The LiCl and LiF interface phases with high interface energy effectively induce the uniform deposition of Li^+ and reduce the overpotential of Li^+ deposition, while the LiZn alloy interface phase accelerates the diffusion of lithium ions. The synergistic effect of the above functional interface phases inhibits the growth of lithium dendrites and stabilizes the interface between the sulfide electrolyte and lithium metal. The hybrid SEI strategy exhibits excellent electrochemical performance on symmetric batteries and all-solid-state batteries. The symmetrical cell exhibits stable cycling performance over long duration over 500 h at 1.0 mA cm^{-2}. Moreover, the $LiNbO_3$@NCM712/$Li_{5.5}PS_{4.5}Cl_{1.5}$/Li-10%ZnF_2 battery exhibits excellent cycle stability at a high rate of 0.5 C, with a capacity retention rate of 76.4% after 350 cycles.

argyrodite electrolytes, ASSLMBs, electrochemical stability, Li-ZnF_2 anode, electrochemical performance

Citation: Wei C, Xiao Y, Wu Z, Liu C, Luo Q, Jiang Z, Li L, Ming L, Yang J, Cheng S, Yu C. Construction of LiCl/LiF/LiZn hybrid SEI interface achieving high-performance sulfide-based all-solid-state lithium metal batteries. *Sci China Chem*, 2024, 67: 1990–2001, https://doi.org/10.1007/s11426-024-2055-4

1 Introduction

The application of non-flammable solid-state electrolytes in solid-state lithium batteries (SSLBs) is widely acknowledged as a prominent candidate for the next generation of energy storage systems [1–5]. This approach primarily mitigates the potential hazards associated with flammable organic liquid electrolytes utilized in traditional lithium-ion batteries [6–8]. Among the array of investigated solid electrolytes, encompassing oxides [9,10], sulfides [11,12], polymers [13–15], and halides [16,17], sulfide solid electrolytes have emerged as particularly auspicious [18,19]. Notably, sulfide solid electrolytes exhibit ionic conductivity comparable to their liquid counterparts while demonstrating outstanding mechanical flexibility [20,21]. This combination of characteristics positions sulfide solid-state electrolytes as among the most promising constituents for the development of high-performance all-solid-state lithium batteries [22,23].

In the realm of sulfide electrolytes, argyrodite electrolytes (Li_6PS_5X, X=Cl, Br, I) have emerged as exemplary representatives due to their high ionic conductivity (>10^{-3} S cm^{-1}), low grain boundary impedance, and com-

*Corresponding author (email: cyu2020@hust.edu.cn)

mendable mechanical properties [24–26]. The integration of solid electrolytes, particularly argyrodites [27,28], with lithium metal anodes is recognized as an optimal approach for achieving high energy density in advanced energy storage systems [29]. Lithium metal anodes exhibit a theoretical specific capacity as high as 3,860 mAh g^{-1} and possess the lowest reduction potential (−3.04 V *vs*. SHE) [30,31]. However, the practical utilization of argyrodite electrolytes faces significant challenges at the interface between the solid electrolyte and lithium metal, particularly in the context of developing high-performance all-solid-state lithium metal batteries (ASSLMBs) [32,33]. On one hand, argyrodite electrolytes are prone to decomposition at lower potentials, leading to undesirable redox reactions with the lithium metal anode and the generation of unstable by-products such as Li_2S [34,35]. The presence of these by-products hinders the ion conduction, increasing the interface impedance, and thereby impacting the electrochemical performance of the battery [36]. On the other hand, the inevitable growth of lithium dendrites poses a formidable challenge [37,38]. Lithium dendrites tend to propagate along the grain boundaries of argyrodite electrolytes, causing internal short circuits in the battery and diminishing the cycle life of ASSLMBs [39,40]. Addressing the interfacial issues between argyrodite electrolytes and lithium metal anodes is imperative for realizing the practical potential of argyrodite electrolytes in the context of high-performance ASSLMBs [41,42].

To alleviate the problems of side reactions at the interface between the argyrodite electrolyte and lithium metal and inhibit the growth of lithium dendrites, several effective strategies have been proposed to improve these problems, including element doping, surface engineering, interface engineering. Wei *et al*. [43] introduced Sb and O elements at the P and S sites in the $Li_{5.5}PS_{4.5}Cl_{1.5}$ sulfide electrolyte, respectively, to form a Li-Sb alloy at the anode interface, which induced the uniform deposition of lithium ions, accelerated the migration of lithium ions at the anode interface, and achieved a stable lithium metal/solid electrolyte (Li/SE) interface. Sun's group [44] used MLD technology to modify a functional intermediate layer on the surface of lithium metal, which also improved the compatibility of sulfide solid electrolytes with lithium metal. In the research of interface engineering between the sulfide electrolyte and lithium metal, some people have also significantly improved the performance of solid-state batteries by *in-situ* forming an interface layer of LiF and LiI between the lithium metal and sulfide electrolyte to inhibit the growth of lithium dendrites [45]. It is worth noting that these strategies together constitute a stable interface of Li/SE. Its overall goal is to alleviate side reactions, inhibit the growth of lithium dendrites, and finally form a stable solid electrolyte interface (SEI). Recent studies suggest that lithium halides (LiX, where X = F, Cl, Br, I) with high interfacial energy contribute to enhanced interface stability and the inhibition of lithium dendrite growth [46,47]. Furthermore, alloying elements introduced as stabilizing components at the solid electrolyte/lithium metal interface exhibit favorable lithium affinity and rapid lithium diffusion capabilities, effectively accelerating their migration at the interface, reducing localized current density, and enhancing interface stability [48–50]. Despite the advancements in individual strategies, the construction of a hybrid SEI at the interface, where both high interfacial energy LiX and LiM alloy with rapid lithium ion diffusion coefficients are simultaneously introduced, remains relatively underexplored. The efficacy and potential advantages of such a hybrid SEI, in comparison to a single SEI, are yet to be conclusively determined.

In this work, we propose a design strategy of a hybrid SEI interface to improve the interfacial compatibility between the $Li_{5.5}PS_{4.5}Cl_{1.5}$ sulfide electrolyte and lithium metal. The Li-ZnF_2 anode with rich LiF and LiZn interfaces was obtained by the reaction of ZnF_2 and molten lithium, and the Li-ZnF_2 anode and $Li_{5.5}PS_{4.5}Cl_{1.5}$ electrolyte further induced the *in-situ* formation of LiCl SEI at the interface. The hybrid SEI can effectively induce the uniform deposition of lithium ions to accelerate the diffusion of lithium ions and inhibit the growth of lithium dendrites. Due to the improved stability of the interface between the $Li_{5.5}PS_{4.5}Cl_{1.5}$ electrolyte and the lithium metal anode, the design of the hybrid SEI significantly increased the critical current density (CCD) of $Li_{5.5}PS_{4.5}Cl_{1.5}$ to 2.9 mA cm^{-2}. In addition, the Li-ZnF_2 anode has cycled stably for more than 500 h at 1.0 mA cm^{-2} in the Li-10%ZnF_2/LPSC/Li-10%ZnF_2 symmetric cell. The ASSLMBs with the Li-10 % ZnF_2 anode can be stably cycled at 0.5 C over 500 cycles.

2 Results and discussion

The Li-ZnF_2 composite lithium anode is synthesized by adjusting the proportion of ZnF_2 powder in lithium metal, as shown in Figure 1a. Usually, ZnF_2 powder is poured into molten lithium on a heating table, stirred and mixed for some time, and converted into LiZn alloy and LiF. After cooling, it is rolled to a uniform thickness of foil. The X-ray diffraction (XRD) pattern of the Li-ZnF_2 anode shows that it is mainly composed of Li, Li-Zn alloy, and LiF (Figure 1b). Furthermore, X-ray photoelectron spectroscopy (XPS) was employed to examine the elemental makeup and valence level of the Li-10% ZnF_2 on the surface. Figure 1c, d displays the distinct peaks of Zn and F elements on the Li-10% ZnF_2 composite anode's surface. The Zn 2p spectrum reveals two peaks near Zn^0 at 1,021.5 eV and 1,045.0 eV [51], which can be attributed to the Zn^{2+} reduction to Zn^0, primarily corresponding to Li-Zn, likely due to the reduction of Zn^{2+} to Zn^0, mainly linked to Li-Zn, while the 684.3 eV peak in the F 1s

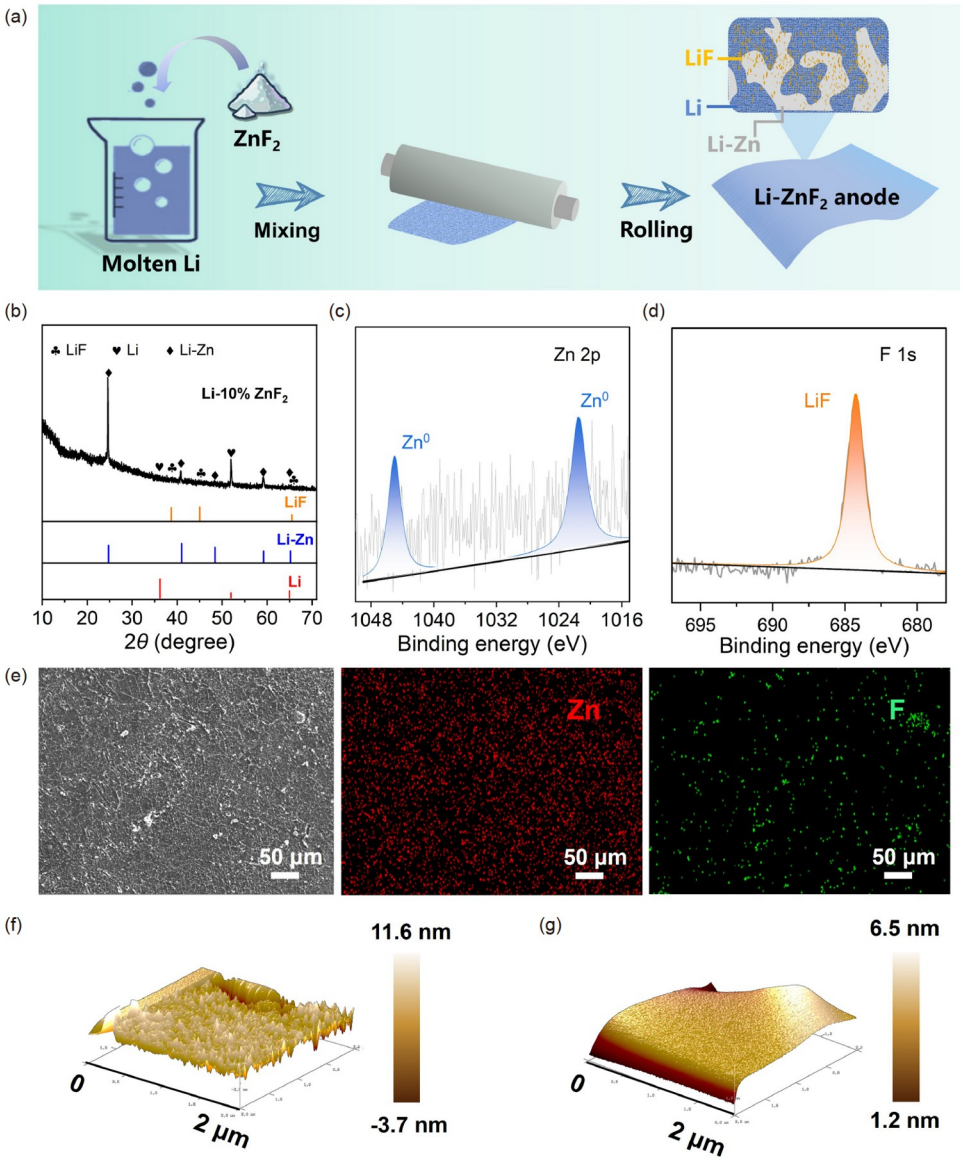

Figure 1 (a) Schematic fabrication process of the Li-x%ZnF_2 (x = 0, 5, 10, and 20) anode. (b) XRD pattern of the Li-10%ZnF_2 composite. The XPS spectra of (c) Zn 2p and (d) F 1s of the Li-10%ZnF_2 anode. (e) The SEM image of the obtained Li-10%ZnF_2 and the corresponding EDS mapping image. 3D AFM images (2 μm×2 μm) of (f) pristine Li and (g) Li-10%ZnF_2 anode (color online).

spectrum corresponds to the LiF phase [52]. The above results are consistent with the XRD results. Scanning electron microscopy (SEM) and energy-dispersive spectroscopy (EDS) images of the Li-ZnF_2 anode show that Zn and F elements are evenly distributed in the composite electrode (Figure 1e). Finally, the morphology of the anode was measured by atomic force microscopy (AFM). The roughness of the composite lithium metal anode was unexpectedly reduced, and the Li–ZnF_2 electrode was smoother and more uniform than the bare Li foil (Figure 1f, g).

To further study the interface and electrochemical stability of bare lithium metal and composite lithium metal anodes with sulfide electrolytes, the chlorine-rich lithium argyrodite electrolyte of $Li_{5.5}PS_{4.5}Cl_{1.5}$ (LPSC) was first prepared by a ball-milling-sintering process. The XRD pattern index to the pure Li_7PS_6 argyrodite target phase [53] shows a cubic structure with a space group of $F-43m$ (Figures S1, S2). Due to the special spatial structure, lithium-ion transport exhibits a very large advantage. The AC impedance was tested using stainless steel as a blocking electrode, and the ionic conductivity was calculated to be as high as 8.2 mS cm^{-1} (Figure S3). The CCD can be used as an effective measure to measure the effect of dendritic inhibition. To evaluate the inhibition of the growth of lithium dendrites in the prepared Li-ZnF_2 composite anodes, these Li-ZnF_2 composite lithium anodes are combined with the LPSC electrolyte to form symmetric batteries Li-x%ZnF_2/LPSC/Li-x%ZnF_2 and tested for CCD. With the increase of current density, the plating/

stripping overpotential of all Li-*x*%ZnF_2/LPSC/Li-*x*%ZnF_2 batteries gradually increases. When the current density increases to 0.5 mA cm^{-2} (0.5 mAh cm^{-2}), the voltage of the Li/LPSC/Li battery drops sharply, followed by a short circuit, which is due to the penetration of dendrites into the LPSC solid electrolyte (Figure 2a). In contrast, Li-5%ZnF_2/LPSC/Li-5%ZnF_2, Li-10%ZnF_2/LPSC/Li-10%ZnF_2, and Li-20%ZnF_2/LPSC/Li -20%ZnF_2 can only be observed when the current density is increased to 1.1, 2.9 and 2.4 mA cm^{-2}, respectively (Figure 2b–d). The Li-10% ZnF_2 composite anode stand out for its exceptional electrochemical performance for lithium metal in symmetrical batteries, and then Li-10% ZnF_2 is selected for further study.

To further verify the superiority of the composite lithium metal anode, the discharge and charge test results of Li/LPSC/Li symmetrical battery and Li-10%ZnF_2/LPSC/Li-10%ZnF_2 symmetrical battery at different current densities and area capacities were compared, and the time-dependent electrochemical impedance spectroscopy (EIS) was conducted. Initially, in the initial 40 h cycle of the constant current charge/discharge test, the overpotential of the two is not much different, which may be related to the stable passivation layer formed at the interface between LPSC electrolyte and lithium metal. However, as the current density increases to 0.3 mA cm^{-2}, the Li-10%ZnF_2/LPSC/Li-10%ZnF_2 symmetrical battery has some advantages in the overpotential, and its overpotential is gentler and smaller. Subsequently, when the current density continues to increase to 1.0 mA cm^{-2}, Li/LPSC/Li exhibits very unstable lithium-ion plating/stripping, and the short circuit occurs quickly. On the contrary, the Li-10%ZnF_2/LPSC/Li-10% ZnF_2 symmetrical battery maintains a relatively stable plating/stripping, and the overpotential remains stable and low (Figure 3a). In addition, through the time-dependent EIS, it can be seen that the interface impedance of Li/LPSC/Li changes obviously with time, especially at a large current density. The impedance increase is very obvious, while Li-10%ZnF_2/LPSC/Li-10%ZnF_2 always maintains a stable interface impedance change, which proves that at a large current density, the Li/LPSC interface will undergo a large interface deterioration, and the formation of interface by-products such as poor ionic conductors will hinder the migration of lithium ions (Figure S4). To better show the advantages of Li-10%ZnF_2/LPSC/Li-10%ZnF_2, its long cycle performance at high current density and area capacity was tested. Li/LPSC/Li unexpectedly showed a very uneven overpotential change and short-circuited quickly. In contrast, Li-10%ZnF_2/LPSC/Li-10%ZnF_2 has a stable cycle for 500 h (Figure 3b). From the local amplification diagram in Figure 3c, its overpotential remains stable, and it still maintains a small overpotential (45 mV) at 500 h. Besides, the Tafel slope was calculated on the symmetrical cells, and the exchange current density of the two anodes was calculated. The exchange current density of the Li-10%ZnF_2/LPSC/Li-10% ZnF_2 composite anode was 151.4 μA cm^{-2}, which was about 2.5 times as high as that of the bare Li anode. (Figure 3d, e) This difference indicates that the stable Li-10%ZnF_2/LPSC interface is conducive to rapid lithium-ion transport and charge transfer. In other words, compared with the single SEI (LiCl) interface of Li/SE, the SEI composed of LiCl, LiF, and LiZn alloy at the Li-10%ZnF_2/LPSC interface can effectively induce the plating/stripping of lithium ions at the anode interface, re-

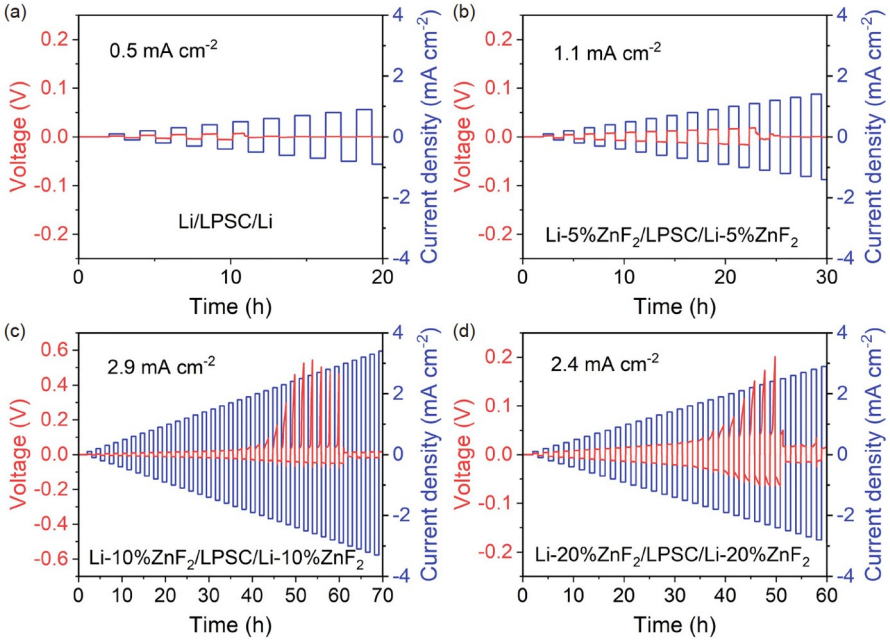

Figure 2 The critical current densities (CCD) measurements of (a) Li/$Li_{5.5}PS_{4.5}Cl_{1.5}$/Li, (b) Li-5%ZnF_2/$Li_{5.5}PS_{4.5}Cl_{1.5}$/Li-5%ZnF_2, (c) Li-10%ZnF_2/$Li_{5.5}PS_{4.5}Cl_{1.5}$/Li-10%ZnF_2, (d) Li-20%ZnF_2/$Li_{5.5}PS_{4.5}Cl_{1.5}$/Li-20%ZnF_2 (color online).

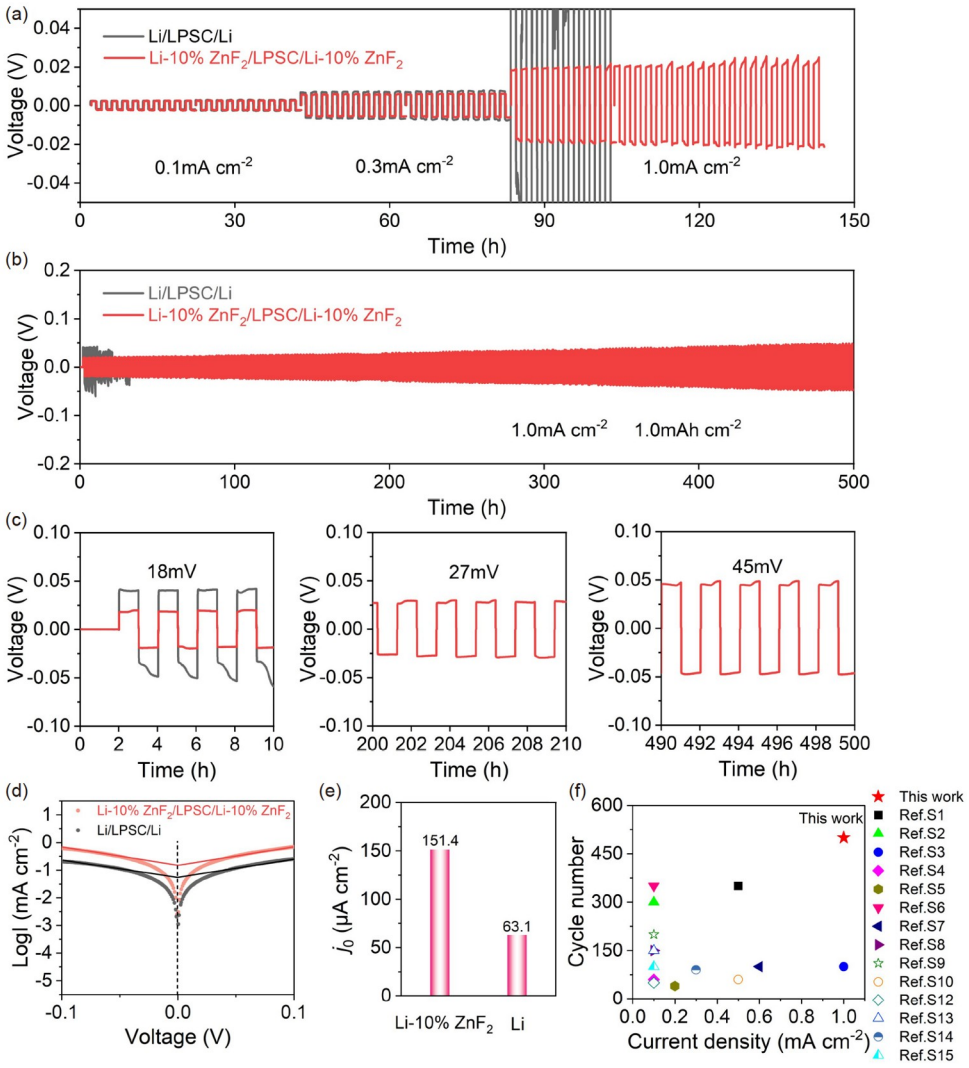

Figure 3 (a) The galvanostatic lithium stripping/plating performances of Li/LPSC/Li and Li-10%ZnF_2/LPSC/Li-10%ZnF_2 symmetric cells cycled at 0.1 mA cm^{-2}, 0.3 mA cm^{-2}, 1.0 mA cm^{-2}. (b) Galvanostatic cycling of Li plating/stripping profiles and (c) partial enlarged detail in the Li/LPSC/Li cell and the Li-10%ZnF_2/LPSC/Li-10%ZnF_2 cell at 1.0 mA cm^{-2}. (d) Tafel plots and (e) calculated exchange current density of Li/LPSC/Li, Li-10%ZnF_2/LPSC/Li-10%ZnF_2 symmetric cells between −100 and 100 mV at a scan rate of 1 mV s^{-1}. (f) Comparison of long cycle performance of lithium-lithium symmetric batteries with sulfide electrolytes (color online).

duce the local current density at the anode interface, inhibit the growth of lithium dendrites, and accelerate the migration and diffusion of lithium ions at the interface. In order to further confirm the advantages of the hybrid SEI interface, Li-10% LiF and Li-10% LiZn composite lithium metal anodes were obtained by reacting molten metal lithium with PTFE and Zn metals respectively to construct a single SEI interface (LiF or LiZn). It was found by CCD test that a single SEI interface phase can also improve the CCD of the battery, where that of Li-10%LiF /LPSC/Li-10%LiF is 1.2 mA cm^{-2} and that of Li-10% LiZn/LPSC /Li-10%LiZn is 1.4 mA cm^{-2} (Figure S5). In comparison, hybrid SEI (LiCl/LiF/LiZn) still has obvious advantages in suppressing lithium dendrites. In addition, we compared the previously reported solid-state batteries (Figure 3f), where Li-10%ZnF_2/LPSC interface improvement exhibits particularly attractive effects at high current densities and long cycles (Table S1).

Furthermore, two different lithium anodes, $LiNbO_3$@$LiNi_{0.7}Mn_{0.2}Co_{0.1}O_2$ cathode ($LiNbO_3$@NCM712) and the $Li_{5.5}PS_{4.5}Cl_{1.5}$ solid electrolyte, were used to prepare and test ASSLMBs for their electrochemical performances. The assembled batteries were tested at different charge–discharge C rates, ranging from 3.0 V to 4.2 V (*vs.* Li^+/Li^0). As shown in Figure 4a, from the voltage–capacity curve, it can be seen that the Li-10%ZnF_2 composite bare lithium anode has a lower charging platform and a higher discharge platform. Compared with the bare lithium anode, the Li-10%ZnF_2 composite lithium anode can achieve higher discharge-specific capacity (150.9 mAh g^{-1} *vs.* 114.4 mAh g^{-1}) and higher Coulombic efficiency (72.8% *vs.* 66.4%) in the first cycle. In

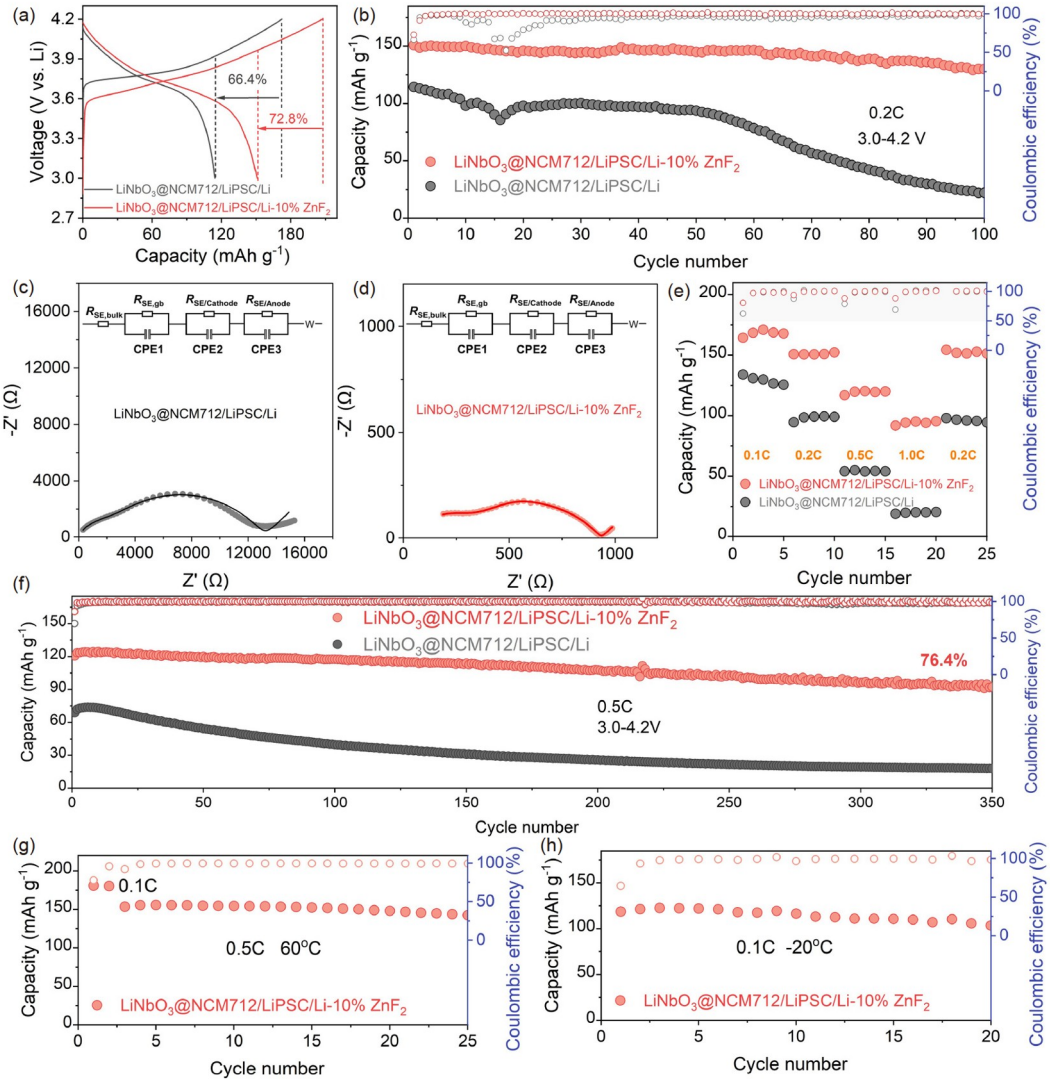

Figure 4 (a) The initial charge-discharge curves and (b) cycling performances of the $LiNbO_3$@NCM712/LPSC/Li and $LiNbO_3$@NCM712/LPSC/Li-10% ZnF_2 all-solid-state lithium metal batteries when cycled at 0.2 C between 3.0 and 4.2 V (*vs.* Li^+/Li^0). EIS spectra of (c) $LiNbO_3$@NCM712/LPSC/Li and (d) $LiNbO_3$@NCM712/LPSC/Li-10%ZnF_2 before and after 100 cycles when cycled at 0.2 C. (e) The rate capability of the $LiNbO_3$@NCM712/LPSC/Li and $LiNbO_3$@NCM712/LPSC/Li-10%ZnF_2 batteries. (f) The long-term cycling performances of the $LiNbO_3$@NCM712/LPSC/Li and $LiNbO_3$@NCM712/LPSC/Li-10%ZnF_2 all-solid-state lithium metal batteries when cycled at 0.5 C. The cycling performances of the $LiNbO_3$@NCM712/LPSC/Li-10%ZnF_2 battery when cycled at (g) 60 °C, and (h) −20 °C (color online).

addition, the use of Li-10%ZnF_2 composite lithium anode still maintains a high-capacity output and maintains a stable cycle during the subsequent cycle. After 100 cycles, the discharge-specific capacity is 129.9 mAh g^{-1}, and the capacity retention rate is 86.1%. However, with the use of bare lithium anode, the battery capacity is significantly lower and the capacity decreases significantly with the increase in the number of cycles. After 100 cycles, the capacity is only 22.1 mAh g^{-1}, and the capacity retention rate is 19.3% (Figure 4b). As shown in Figure S6, these batteries show a similar Nyquist curve before cycling. The advantage of Li-10%ZnF_2 anode may be due to the better contact between Li-10%ZnF_2 composite lithium metal and solid electrolyte. As shown in Figure 4c, d, the total resistance of all batteries increased after 100 cycles. Compared with $LiNbO_3$@NCM712/LPSC/Li-10% ZnF_2, $LiNbO_3$@NCM712/LPSC/Li battery has a larger total resistance. Alterations noted in the EIS spectra suggest that employing a composite lithium metal anode can improve the kinetics of lithium-ion transport in the constructed ASSLMB and is more compatible with the sulfide-based electrolyte. Subsequently, the EIS spectrum was analyzed by an impedance fitting tool. It can be seen that it consists of five parts: bulk impedance of solid electrolyte ($R_{SE,\ bulk\ phase}$), grain boundary resistance of solid electrolyte ($R_{SE,\ gb}$), interface impedance of cathode ($R_{SE/cathode}$) and anode ($R_{SE/anode}$) between electrolytes, and diffusion impedance. The difference in impedance changes between the two batteries are entirely attributed to the anode side because

all other components in the battery configuration are the same. For the cycled $LiNbO_3$@NCM712/LPSC/Li battery, the $R_{SE/anode}$ increased significantly to 11,800.0 Ω, indicating that a strong side reaction occurred between the $Li_{5.5}PS_{4.5}Cl_{1.5}$ electrolyte and lithium metal anode during 100 cycles. By contrast, the $R_{SE/anode}$ of $LiNbO_3$@NCM712/LPSC/Li-10%ZnF_2 battery is only 622.0 Ω, which is much smaller, and the result corresponds to the battery performance. In addition, the rate capability of these two batteries was compared. As shown in Figure 4e, the battery with the Li-10%ZnF_2 anode has higher discharge-specific capacity and Coulombic efficiency than the Li anode-based battery at different C-rates. In detail, the $LiNbO_3$@NCM712/$Li_{5.5}PS_{4.5}Cl_{1.5}$/Li battery achieves discharge rates of 130.8 mAh g^{-1} at 0.1 C, 99.4 mAh g^{-1} at 0.2 C, 55.0 mAh g^{-1} at 0.5 C, and 20.5 mAh g^{-1} at 1.0 C, respectively, and maintains a discharge capacity of 95.6 mAh g^{-1} once the rate returns to 0.2 C. The $LiNbO_3$@NCM712/LPSC/Li-10%ZnF_2 battery, however, offers significantly greater discharge capacities, with capacities of 170.9 mAh g^{-1} at 0.1 C, 150.9 mAh g^{-1} at 0.2 C, 120.3 mAh g^{-1} at 0.5 C, and 95.2 mAh g^{-1} at 1.0 C, in that order, and sustains a discharge capacity of 151.5 mAh g^{-1} once the rate returns to 0.2 C. Subsequently, a long cycle test was carried out at a higher charge–discharge rate (0.5 C), as shown in Figure 4f, and the battery using the Li-10%ZnF_2 composite anode showed excellent cycling performance. The initial discharge-specific capacity is 120.6 mAh g^{-1}, which remains stable after 350 cycles, and the capacity retention rate is 76.4%. By contrast, the battery using Li metal anode exhibits poor electrochemical performance and cycle stability. The first cycle discharge-specific capacity is only 68.7 mAh g^{-1}, and the capacity decays suddenly after 350 cycles, and the capacity retention rate is only 26.1%. In addition, the $LiNbO_3$@NCM712/LPSC/Li-10%ZnF_2 battery is placed in a more extreme operating environment. When the temperature rises to 60 °C, the high temperature can accelerate the migration of lithium ions and achieve higher discharge-specific capacity. At 0.1 C, the first cycle discharge is 180.7 mAh g^{-1}, and the discharge-specific capacity of 153.4 mAh g^{-1} is achieved in the 3rd cycle, and it runs stably for 25 cycles. Subsequently, when the temperature is reduced to −20 °C, the low temperature will inhibit the migration of lithium ions. Although its discharge-specific capacity is reduced, it can still achieve 118.5 mAh g^{-1} cycles at 0.1 C and be stabilized 20 cycles. The above results show that $LiNbO_3$@NCM712/LPSC/Li-10%ZnF_2 ASSLMB has excellent electrochemical performance. The design of the composite SEI interface achieves excellent electrochemical performance because the presence of LiF and LiCl in the composite SEI interface can inhibit the growth of lithium dendrites, and LiZn alloy can increase the migration rate of lithium ions at the solid electrolyte/lithium anode interface.

ASSLMBs' interface development with lithium metal and Li-10%ZnF_2 anodes involved tracking the impedance variations in both batteries under varying charge of states (SOC) through *in-situ* EIS. This impedance was then separated using the distribution of relaxation time (DRT) method to examine each component's impedance progression. As shown in Figure S7, during the charging process, with the increase of SOC, the impedance decreases first and then increases. During the discharge process, except for the sudden increase of impedance at 3.0 V, the other impedances decrease with the increase of SOC. This is consistent with the impedance variation of ASSLMBs before. It is worth noting that the impedance of the $LiNbO_3$@NCM712/LPSC/Li-10%ZnF_2 battery is much smaller than that of the $LiNbO_3$@NCM712/LPSC/Li battery during the entire charging/discharging process. Previous publications state that the impedance is a result of several components, including the solid electrolyte bulk impedance and grain boundary impedance, cathode/electrolyte, anode/electrolyte, and tail of the Warburg impedance [31]. The impedance of each part is displayed by DRT technology. Compared with the Li/SE part, in the ASSLMBs system, the peak is mainly presented between 10^{-1}–10^{0} s. In either charging or discharging, it can be seen that the Li/SE impedance of the $LiNbO_3$@NCM712/LPSC/Li battery shows a continuous change, while the impedance of this part of the $LiNbO_3$@NCM712/LPSC/Li-10%ZnF_2 battery remains stable (Figure 5a). In addition, by showing the DRT curve through the contour map, it is more intuitive to show that the bare lithium metal battery shows a large interface impedance, especially the Li/SE interface impedance (Figure 5b). This is mainly due to the unstable interface between Li metal and sulfide electrolyte, resulting in uneven lithium deposition during lithium plating/stripping of lithium anode, which increases the interface impedance. By contrast, the Li-10%ZnF_2 anode can induce the uniform deposition of lithium ions due to the presence of composite SEI, maintaining a stable Li/SE interface.

XPS was used to study the change of charge state of $Li_{5.5}PS_{4.5}Cl_{1.5}$ electrolyte before and after cycling with two anodes (Li and Li-10%ZnF_2). As shown in Figure 6a, the peaks attributed to PS_4^{3-} were detected at 160.68 eV in the S 2p and 131.03 eV in the P 2p spectra, and no additional peaks were detected, which verified the high purity phase of $Li_{5.5}PS_{4.5}Cl_{1.5}$ [54]. For the $LiNbO_3$@NCM712/LPSC/Li battery, after the cycle of $Li_{5.5}PS_{4.5}Cl_{1.5}$ electrolyte and lithium metal anode, in addition to the PS_4^{3-} peak, the S 2p spectrum also detected clear signals of Li_2S, Li_2S_x and P_2S_x. At the same time, the P 2p spectrum also detected substances such as P_2S_x and Li_3P, indicating that a strong redox side reaction occurred between the lithium metal and the $Li_{5.5}PS_{4.5}Cl_{1.5}$ electrolyte (Figure 6b). By contrast, for the $LiNbO_3$@NCM712/LPSC/Li-10%ZnF_2 battery assembled by the $Li_{5.5}PS_{4.5}Cl_{1.5}$ electrolyte and Li-10%ZnF_2 anode, weak by-product signals such as Li_2S_x, Li_2S, and P_2S_x were

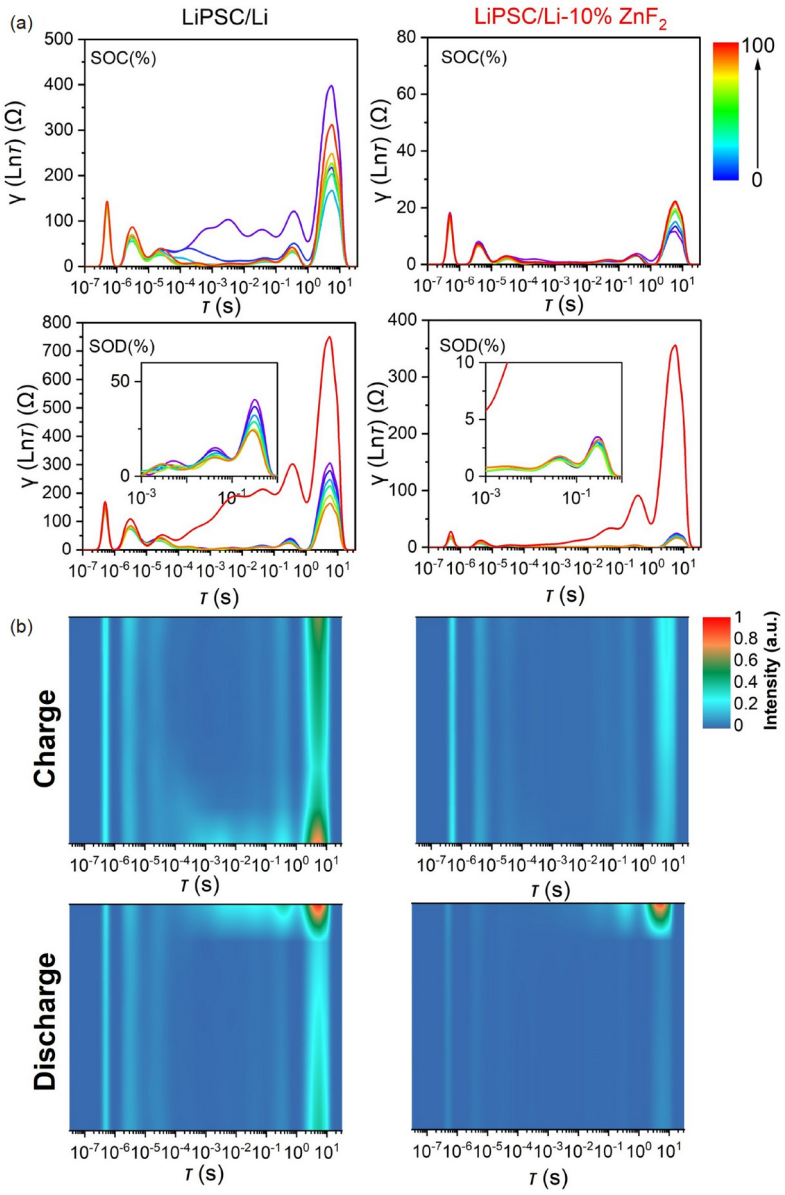

Figure 5 (a, b) The distribution of relaxation time (DRT) analysis for the assembled $LiNbO_3$@NCM712/$Li_{5.5}PS_{4.5}Cl_{1.5}$/Li and $LiNbO_3$@NCM712/$Li_{5.5}PS_{4.5}Cl_{1.5}$/Li-10%ZnF_2 batteries under different states of charge (SOC) and states of discharge (SOD) during the 1st cycle. All tests were performed at room temperature (color online).

detected after the cycle, which proved that the Li-10%ZnF_2 anode showed better interfacial compatibility with $Li_{5.5}PS_{4.5}Cl_{1.5}$ than the bare lithium anode (Figure 6c). To more accurately compare the difference between the two anodes and LPSC compatibility, a semi-quantitative analysis method was used. As shown in Figure 6d, after the $Li_{5.5}PS_{4.5}Cl_{1.5}$ electrolyte and Li anode cycle, in either S 2p or P 2p spectrum, the proportion of the main phase PS_4^{3-} is only about 46 %; meanwhile, after the $Li_{5.5}PS_{4.5}Cl_{1.5}$ electrolyte and Li-10%ZnF_2 anode cycle, the proportion of PS_4^{3-} is as high as 82%, which proves that the $Li_{5.5}PS_{4.5}Cl_{1.5}$ has a large degradation with Li anode during the cycle, and can significantly reduce the degree of side reactions with Li-10% ZnF_2 anode. In addition, the types of by-products produced in $Li_{5.5}PS_{4.5}Cl_{1.5}$/Li-10%ZnF_2 are also significantly less. The above results prove that compared with bare metal lithium, Li-10%ZnF_2 anode can significantly reduce the interface side reaction with sulfide electrolytes and reduce the degradation of sulfide electrolytes, which corresponds to the electrochemical performance in Figure 4.

To further elucidate the morphological variations observed on the surface of the pristine lithium metal and Li-10%ZnF_2 anodes, comprehensive investigations were conducted using SEM and EDS mapping on both the freshly prepared and cycled anodes. Before cycling, the SEM images in Figure 7a reveal a smooth and flat surface for the bare lithium metal. By contrast, Figure 7b illustrates the Li-10%ZnF_2 anode exhibiting a consistently uniform and densely deposited

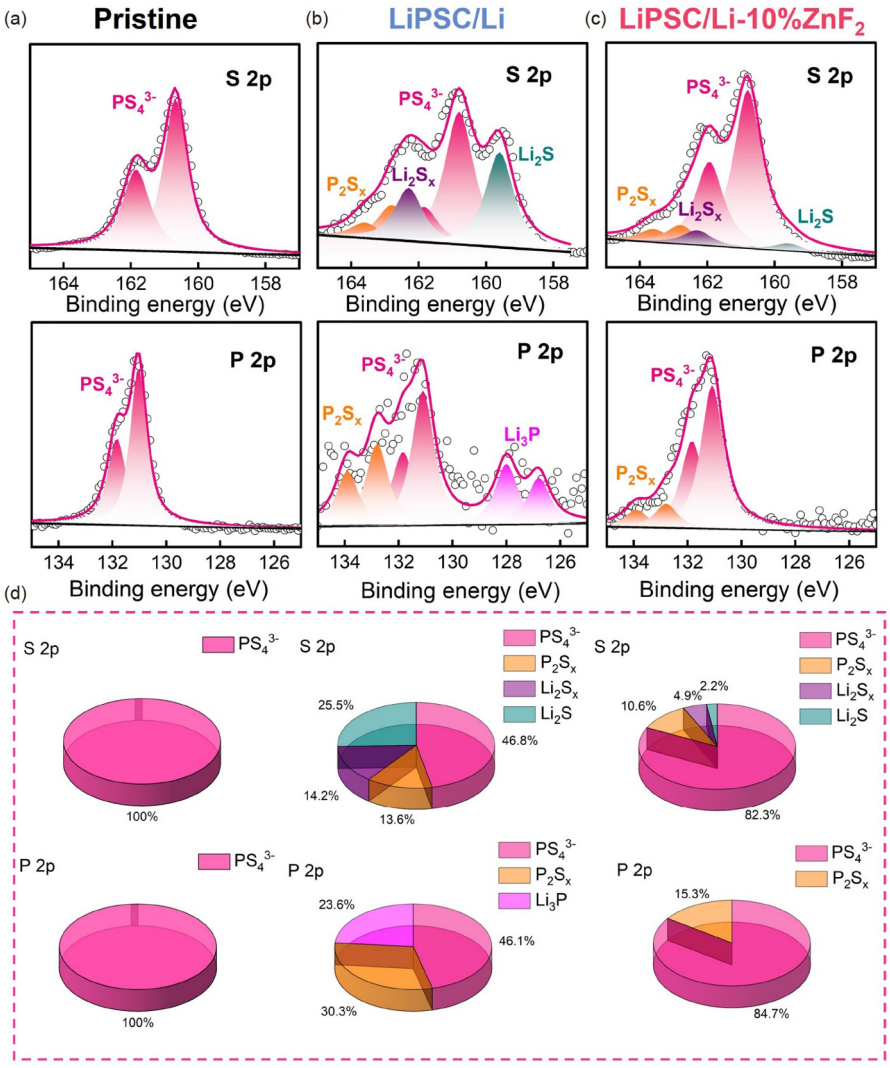

Figure 6 XPS results of the $Li_{5.5}PS_{4.5}Cl_{1.5}$ electrolyte from the $LiNbO_3$@NCM712/$Li_{5.5}PS_{4.5}Cl_{1.5}$/Li and $LiNbO_3$@NCM712/$Li_{5.5}PS_{4.5}Cl_{1.5}$/Li-10%ZnF_2 all-solid-state lithium metal batteries before and after 100 cycles. (a) The S 2p spectra and P 2p spectra of the $Li_{5.5}PS_{4.5}Cl_{1.5}$ electrolyte before cycling. The S 2p and P 2p spectra of the $Li_{5.5}PS_{4.5}Cl_{1.5}$ electrolyte cycled with the (b) bare lithium metal and (c) Li-10%ZnF_2. (d) The pie distribution diagram of the above components (color online).

coverage on its surface. These dense and uniform materials are mainly composed of LiF and LiZn alloys, which have been proved in Figure 1e. After 100 cycles of cycling at 0.2 C in the assembled $LiNbO_3$@NCM712/LPSC/Li battery, Figure 7c shows that the surface of the lithium metal anode has significant cracks and depressions. Corresponding EDS mapping reveals impurities primarily composed of multiple P, S, and Cl elements with homogeneous distributions, associated with the formation of Li_2S, P_2S_x, and LiCl phases resulting from side reactions between the lithium metal and the $Li_{5.5}PS_{4.5}Cl_{1.5}$ electrolytes. By stark contrast, the Li-10% ZnF_2 anode maintains an intact surface morphology after an identical number of cycles in the $LiNbO_3$@NCM712/LPSC/Li-10%ZnF_2 battery, as evidenced by SEM images in Figure 7d. The related EDS mapping confirms an even spread of LiZn and LiF across the lithium metal anode's surface, including the remnants of the stripped $Li_{5.5}PS_{4.5}Cl_{1.5}$ electrolyte. It is worth noting that, as shown by the surface scanning of the Cl element, there is a dense and uniform LiCl interface on the Li-10%ZnF_2 anode surface in addition to the LiF and LiZn interfaces, which further confirms the presence of LiCl in the hybrid interface. Compared with $Li_{5.5}PS_{4.5}Cl_{1.5}$/Li, the Cl at the interface of $Li_{5.5}PS_{4.5}Cl_{1.5}$/Li-10%ZnF_2 is significantly more uniform and denser, indicating that the ZnF_2 treatment of lithium metal strategy not only induces the formation of LiF and LiZn interfaces, but also induces the formation of more LiCl at the anode interface. According to the above results, the deposition behavior of Li^+ on the lithium metal anode and Li-10%ZnF_2 anode is shown in Figure 7e. For the bare lithium electrode, due to the serious interfacial side reaction with the $Li_{5.5}PS_{4.5}Cl_{1.5}$ electrolyte and the large nucleation overpotential of lithium, it is easy to

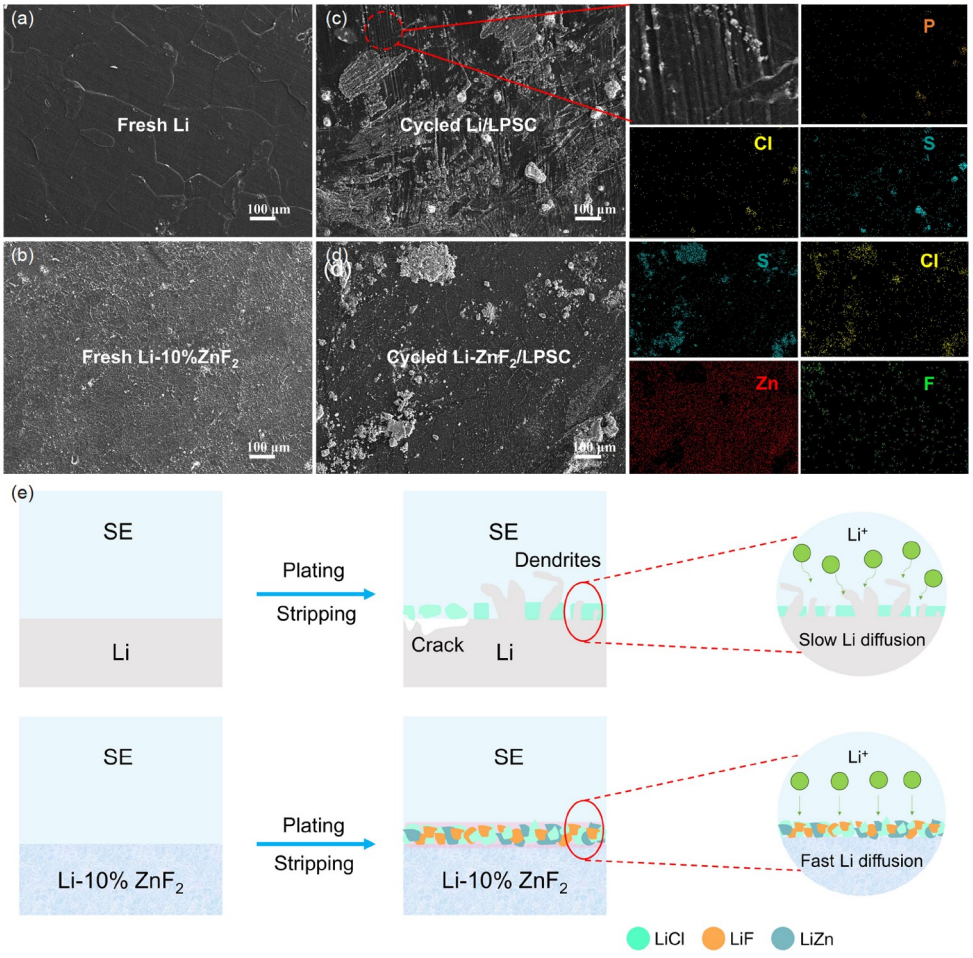

Figure 7 SEM images of the surface sections of (a) the fresh lithium metal and (b) the fresh Li-10%ZnF_2 composite. (c) The SEM images and corresponding EDS mapping of the lithium metal in the assembled $LiNbO_3$@NCM712/$Li_{5.5}PS_{4.5}Cl_{1.5}$/Li solid-state lithium metal batteries cycled at 0.2 C between 3.0 and 4.2 V (*vs.* Li^+/Li^0) after 100 cycles under room temperature. (d) The 10%ZnF_2-modified lithium metal in the assembled $LiNbO_3$@NCM712/$Li_{5.5}PS_{4.5}Cl_{1.5}$/Li-10%SnF_2 solid-state lithium metal batteries cycled at 0.2 C between 3.0 and 4.2 V (*vs.* Li^+/Li^0) after 100 cycles under room temperature and the corresponding EDS mapping. (e) Schematic of the lithium stripping and plating processes for the $Li_{5.5}PS_{4.5}Cl_{1.5}$/Li and $Li_{5.5}PS_{4.5}Cl_{1.5}$/Li-10%ZnF_2 interface (color online).

form lithium dendrites at the interface. Even if LiCl is used as a passivation layer to inhibit the growth of dendrites, the growth of LiCl is not uniform and this single SEI inhibition is relatively weak. In addition, the slow lithium diffusion kinetics aggravates the uneven deposition of lithium. By contrast, the lithium affinity of LiZn alloy in the Li-10%ZnF_2 electrode reduces the nucleation barrier of lithium, and the high diffusion coefficient ensures the rapid diffusion of lithium at the interface. In addition, LiF and LiCl with the high interfacial energy can effectively inhibit the growth of lithium dendrites. Therefore, since the hybrid SEI can effectively adjust the uniform lithium plating/stripping behavior of the Li-10%ZnF_2 electrode, a stable cycle of the ASSLMB can be achieved.

In addition, the working mechanism of hybrid SEI on lithium dendrite inhibition was confirmed by density functional theory (DFT). Firstly, because lithium ions have the lowest surface energy under the aforementioned migration path, LiF (001), LiCl (001), and LiZn (110) were chosen as surface models to investigate the migration kinetics of Li^+ on their surfaces (Figure 8a–c). Subsequently, the kinetic energy barrier of Li^+ diffusion at the most stable adsorption site was then investigated using the climbing image-nudged elastic band (CI-NEB) approach. Calculations indicate that the diffusion energy barriers for Li^+ on LiCl, LiF, and LiZn surfaces stand at 0.120 eV, 0.160 eV, and 0.076 eV, respectively (Figure 8d–f). This further confirms that the rapid lithium-ion migration kinetics of LiZn alloy can accelerate the diffusion of lithium ions, while the higher lithium diffusion energy barrier of LiCl and LiF can inhibit the formation of lithium dendrites. In addition, the growth of lithium dendrites is caused by non-uniform nucleation at the interface, and lithium nucleation and growth need to overcome the interface energy. Therefore, the interface energies of hybrid SEI(LiCl+LiF+LiZn/Li) and single SEI(LiCl/Li) with lithium were calculated, respectively (Figure 8g). As shown in

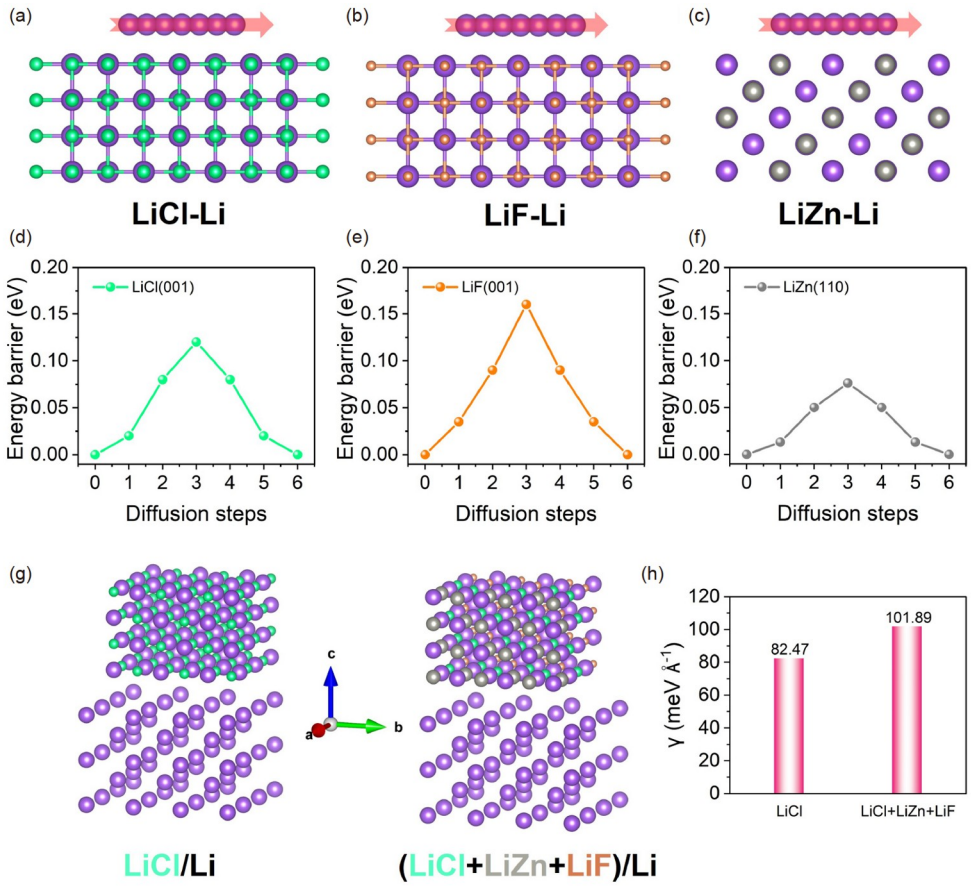

Figure 8 Li^+ migration paths on the (a) LiF (001), (b) LiCl (001), and (c) $Li_{22}Sn_5$ (110) surfaces. The kinetic energy barriers of Li^+ diffusion on the (d) LiF (001), (e) LiCl (001), and (f) $Li_{22}Sn_5$ (110) surfaces. (g) The atomic structure of LiCl/Li, (LiCl+LiZn+LiF) /Li interface. (h) DFT calculation results between the interface energy of Li for LiCl/Li, (LiCl+LiZn+LiF) /Li (color online).

Figure 8h, through the calculation results, compared with a single SEI, the hybrid SEI interface has advantages in effectively inhibiting the formation and growth of lithium dendrites. In other words, the hybrid SEI is capable of restricting lithium dendrite growth at the interfaces with significant lithium diffusion barriers (like LiCl and LiF), and it can hasten lithium-ion movement through the LiZn alloy with a high diffusion coefficient, creating a synergistic impact. This leads to even lithium-ion deposition on the anode side, lessens the overpotential in lithium stripping plating, and results in a more stable Li/SE interface.

3 Conclusions

In summary, a hybrid SEI interface based on LiCl, LiF, and LiZn was constructed at the interface between the sulfide electrolyte and lithium metal anode to improve the interface stability between $Li_{5.5}PS_{4.5}Cl_{1.5}$ electrolyte and lithium metal. The high interface energy of LiF and LiCl in the hybrid SEI can effectively inhibit the growth of lithium dendrites, while the lithophilic LiZn alloy can induce the uniform deposition of lithium ions, reduce the local overpotential and accelerate the diffusion of lithium ions. The hybrid SEI can cooperate with the above SEI functions to achieve a stable solid electrolyte/Li interface. Benefiting from the above characteristics, the Li-10%ZnF_2/LPSC/Li-10%ZnF_2 symmetrical battery exhibits higher CCD (2.9 mA cm^{-2}) and longer cycle stability at the high current density (500 h, 1.0 mA cm^{-2}). In addition, the $LiNbO_3$@NCM712/LPSC/Li-10%ZnF_2 battery exhibits a high discharge-specific capacity of 150.9 mAh g^{-1} at 0.2 C, and exhibits a high-capacity retention rate of 86.1% after 100 cycles, and exhibits excellent cycle stability at a high rate of 0.5 C, with a capacity retention rate of 76.4% after 350 cycles. It still exhibits good electrochemical performance in a wider temperature range (60 °C and −20 °C). Moreover, DFT theoretical calculations further confirmed that the hybrid SEI has a higher interface energy to Li. This work elucidates the role of hybrid SEI in all-solid-state lithium metal batteries and provides an effective idea for constructing a stable Li/SE interface.

Acknowledgements This work was supported by the National Key Research and Development Program of China (2021YFB2500200) and the

National Natural Science Foundation of China (52177214). This work is also supported by China Fujian Energy Devices Science and Technology Innovation Laboratory Open Fund (21C-OP202211). We gratefully acknowledge HUST's Analytical and Testing Center for the technical support.

Conflict of interest The authors declare no conflict of interest.

Supporting information The supporting information is available online at chem.scichina.com and link.springer.com/journal/11426. The supporting materials are published as submitted, without typesetting or editing. The responsibility for scientific accuracy and content remains entirely with the authors.

1 Zhang H, Yu Z, Chen H, Zhou Y, Huang X, Tian B. *J Energy Chem*, 2023, 79: 348–356
2 Luo Q, Ming L, Zhang D, Wei C, Wu Z, Jiang Z, Liu C, Liu S, Cao K, Zhang L, Yu C, Cheng S. *Energy Mater Adv*, 2023, 4: 0065
3 Tufail MK, Zhai P, Jia M, Zhao N, Guo X. *Energy Mater Adv*, 2023, 4: 0015
4 Wei C, Yu C, Chen S, Chen S, Peng L, Wu Y, Li S, Cheng S, Xie J. *Electrochim Acta*, 2023, 438: 141545
5 Luo Q, Yu C, Wei C, Chen S, Chen S, Jiang Z, Peng L, Cheng S, Xie J. *Ceramics Int*, 2023, 49: 11485–11493
6 Xu J, Xiang S, Yi C, Liu X, An L, Wang Z, Jiang H, Cheng GJ. *Energy Mater Adv*, 2023, 4: 0012
7 Chang X, Zhao YM, Yuan B, Fan M, Meng Q, Guo YG, Wan LJ. *Sci China Chem*, 2024, 67: 43–66
8 Xin S, Zhang X, Wang L, Yu H, Chang X, Zhao YM, Meng Q, Xu P, Zhao CZ, Chen J, Lu H, Kong X, Wang J, Chen K, Huang G, Zhang X, Su Y, Xiao Y, Chou SL, Zhang S, Guo Z, Du A, Cui G, Yang G, Zhao Q, Dong L, Zhou D, Kang F, Hong H, Zhi C, Yuan Z, Li X, Mo Y, Zhu Y, Yu D, Lei X, Zhao J, Wang J, Su D, Guo YG, Zhang Q, Chen J, Wan LJ. *Sci China Chem*, 2024, 67: 13–42
9 Ferraresi G, Uhlenbruck S, Tsai CL, Novák P, Villevieille C. *Batteries Supercaps*, 2020, 3: 557–565
10 van den Broek J, Afyon S, Rupp JLM. *Adv Energy Mater*, 2016, 6: 1600736
11 Wei C, Yu C, Peng L, Zhang Z, Xu R, Wu Z, Liao C, Zhang W, Zhang L, Cheng S, Xie J. *Mater Adv*, 2022, 3: 1047–1054
12 Wei C, Yu D, Xu X, Wang R, Li J, Lin J, Chen S, Zhang L, Yu C. *Chem — An Asian J*, 2023, 18: e202300304
13 Wang Z, Shen L, Deng S, Cui P, Yao X. *Adv Mater*, 2021, 33: 2100353
14 Ge Z, Liu X, Zou X, Zhan Y, Luo Y. *J Appl Polym Sci*, 2021, 138: 50945
15 Xu P, Shuang ZY, Zhao CZ, Li X, Fan LZ, Chen A, Chen H, Kuzmina E, Karaseva E, Kolosnitsyn V, Zeng X, Dong P, Zhang Y, Wang M, Zhang Q. *Sci China Chem*, 2024, 67: 67–86
16 Chen S, Yu C, Wei C, Jiang Z, Zhang Z, Peng L, Cheng S, Xie J. *Energy Mater Adv*, 2023, 4: 0019
17 Chen S, Yu C, Luo Q, Wei C, Li L, Li G, Cheng S, Xie J. *Acta Physico Chim Sin*, 2022, 39: 2210032
18 Yang M, Chen L, Li H, Wu F. *Energy Mater Adv*, 2022, 2022: 9842651
19 Wei C, Liu X, Yu C, Chen S, Chen S, Cheng S, Xie J. *Chin Chem Lett*, 2023, 34: 107859
20 Wei C, Chen S, Yu C, Wang R, Luo Q, Chen S, Wu Z, Liu C, Cheng S, Xie J. *Appl Mater Today*, 2023, 31: 101770
21 Wu J, Liu S, Han F, Yao X, Wang C. *Adv Mater*, 2021, 33: 2000751
22 Liang J, Li X, Wang C, Kim JT, Yang R, Wang J, Sun X. *Energy Mater Adv*, 2023, 4: 0021
23 Wang Y, Wang Z, Wu D, Niu Q, Lu P, Ma T, Su Y, Chen L, Li H, Wu F. *eScience*, 2022, 2: 537–545
24 Peng L, Yu C, Zhang Z, Ren H, Zhang J, He Z, Yu M, Zhang L, Cheng S, Xie J. *Chem Eng J*, 2022, 430: 132896
25 Yu C, Zhao F, Luo J, Zhang L, Sun X. *Nano Energy*, 2021, 83: 105858
26 Arnold W, Buchberger DA, Li Y, Sunkara M, Druffel T, Wang H. *J Power Sources*, 2020, 464: 228158
27 Zhao F, Liang J, Yu C, Sun Q, Li X, Adair K, Wang C, Zhao Y, Zhang S, Li W, Deng S, Li R, Huang Y, Huang H, Zhang L, Zhao S, Lu S, Sun X. *Adv Energy Mater*, 2020, 10: 1903422
28 Chen T, Zhang L, Zhang Z, Li P, Wang H, Yu C, Yan X, Wang L, Xu B. *ACS Appl Mater Interfaces*, 2019, 11: 40808–40816
29 Yu C, Ganapathy S, Eck ERH, Wang H, Basak S, Li Z, Wagemaker M. *Nat Commun*, 2017, 8: 1086
30 Wu Z, Yu C, Wei C, Jiang Z, Liao C, Chen S, Chen S, Peng L, Cheng S, Xie J. *Chem Eng J*, 2023, 466: 143304
31 Wei C, Wang R, Wu Z, Luo Q, Jiang Z, Ming L, Zhang L, Lu H, Li G, Li L, Yu C, Cheng S. *Chem Eng J*, 2023, 476: 146531
32 Wu Z, Chen S, Yu C, Wei C, Peng L, Wang HL, Cheng S, Xie J. *Chem Eng J*, 2022, 442: 136346
33 Liu H, Zhu Q, Liang Y, Wang C, Li D, Zhao X, Gao L, Fan LZ. *Chem Eng J*, 2023, 462: 142183
34 Liu G, Weng W, Zhang Z, Wu L, Yang J, Yao X. *Nano Lett*, 2020, 20: 6660–6665
35 Fan Q, Zhang W, Jin Y, Zhang D, Meng X, Peng W, Wang J, Mo J, Liu K, Liu L, Li M. *Chem Eng J*, 2023, 477: 147179
36 Liu H, Zhu Q, Wang C, Wang G, Liang Y, Li D, Gao L, Fan LZ. *Adv Funct Mater*, 2022, 32: 2203858
37 Ge Z, Chen N, Wang R, Ma R, Fan B, Le coq D, Zhang X, Ma H, Xue B. *Chem Eng J*, 2023, 467: 143409
38 Wang JC, Wang PF, Yi TF. *Energy Storage Mater*, 2023, 62: 102958
39 Li J, Li Y, Cheng J, Sun Q, Dai L, Ci N, Li D, Ci L. *J Power Sources*, 2022, 518: 230739
40 Takahashi M, Watanabe T, Yamamoto K, Ohara K, Sakuda A, Kimura T, Yang S, Nakanishi K, Uchiyama T, Kimura M, Hayashi A, Tatsumisago M, Uchimoto Y. *Chem Mater*, 2021, 33: 4907–4914
41 Wu M, Li M, Jin Y, Chang X, Zhao X, Gu Z, Liu G, Yao X. *J Energy Chem*, 2023, 79: 272–278
42 Pang B, Gan Y, Xia Y, Huang H, He X, Zhang W. *Front Chem*, 2022, 10: 837978
43 Wei C, Yu C, Wang R, Peng L, Chen S, Miao X, Cheng S, Xie J. *J Power Sources*, 2023, 559: 232659
44 Wang C, Zhao Y, Sun Q, Li X, Liu Y, Liang J, Li X, Lin X, Li R, Adair KR, Zhang L, Yang R, Lu S, Sun X. *Nano Energy*, 2018, 53: 168–174
45 Xu R, Han F, Ji X, Fan X, Tu J, Wang C. *Nano Energy*, 2018, 53: 958–966
46 Yang S, Takahashi M, Yamamoto K, Ohara K, Watanabe T, Uchiyama T, Takami T, Sakuda A, Hayashi A, Tatsumisago M, Uchimoto Y. *Solid State Ion*, 2022, 377: 115869
47 Xue T, Qian J, Guo X, Chen Y, Yu K, Yu T, Li Y, Li L, Wu F, Chen R. *Sci China Chem*, 2023, 66: 2121–2129
48 Ni Y, Huang C, Liu H, Liang Y, Fan LZ. *Adv Funct Mater*, 2022, 32: 2205998
49 Jiang Z, Peng H, Liu Y, Li Z, Zhong Y, Wang X, Xia X, Gu C, Tu J. *Adv Energy Mater*, 2021, 11: 2101521
50 Wang C, Hao J, Wu J, Shi H, Fan L, Wang J, Wang Z, Wang Z, Yang L, Gao Y, Yan X, Gu Y. *Adv Funct Mater*, 2024, 34: 2313308
51 Wu ZW, Tyan SL, Chen HH, Huang JCA, Huang YC, Lee CR, Mo TS. *Superlattices MicroStruct*, 2017, 107: 38–43
52 Li Z, Jiang X, Lu G, Deng T, Wang R, Wei J, Zheng W, Yang Z, Tang D, Zhao Q, Hu X, Xu C, Zhou X. *Chem Eng J*, 2023, 465: 142895
53 Peng L, Chen S, Yu C, Wei C, Liao C, Wu Z, Wang HL, Cheng S, Xie J. *ACS Appl Mater Interfaces*, 2022, 14: 4179–4185
54 Wei C, Liu C, Xiao Y, Wu Z, Luo Q, Jiang Z, Wang Z, Zhang L, Cheng S, Yu C. *Adv Funct Mater*, 2024, 34: 2314306